Robotica (2025), **43**, pp. 3346–3365
doi:10.1017/S0263574725102452

CAMBRIDGE UNIVERSITY PRESS

RESEARCH ARTICLE

A cable-based synergy drive approach for variable curvature snake-like robots

Baoyue Lu, Shuxin Wang and Lizhi Pan

School of Mechanical Engineering, Tianjin University, Tianjin, China
Corresponding author: Lizhi Pan; Email: melzpan@tju.edu.cn

Received: 16 April 2025; **Revised:** 6 August 2025; **Accepted:** 17 August 2025; **First published online:** 17 September 2025

Keywords: snake-like robot; synergy drive; variable curvature; cable configuration

Abstract

Cable-driven snake-like robots have been widely applied in various fields. However, some of these robots may have poor operational precision and payload capacity. Moreover, an excessive number of motors would increase the complexity of motion control, and the configuration of driving cables at the distal joints is severely limited by the drive system. Therefore, this study introduces a driving model of cable-driven rolling joints through coordinate-based analysis, and proposes a novel two-degree-of-freedom planar synergy drive system to enable variable curvature at the distal joints. A prototype was designed based on the proposed system, which was put into a precision experiment. Two quantifiable parameters were proposed to demonstrate the advantages of the proposed system. The distal joint precision and the driving model precision were employed as indicators to quantify the performance of the prototype. The maximum mean absolute error of the two indicators was 1.52% and 1.88°, respectively, and the maximum root mean square error was 1.66% and 2.02°, respectively. The experimental results demonstrate the feasibility of our approach, which offers increased flexibility in the cable configuration at the distal joints.

1. Introduction

With a high length-to-diameter ratio and excellent flexibility, snake-like robots are widely used in multiple fields, such as medicine and industry [1–5]. Currently, the snake-like robots are mainly actuated by cable-driven systems [6, 7], pneumatic-driven systems [8, 9], and shape memory alloy-driven systems [10]. Among these, cable-driven systems can keep the drive mechanisms away from the distal joints and help downsize the distal joints [11, 12], making them particularly favored in areas with limited space.

According to the joint configuration, cable-driven snake-like robots may have a continuous configuration or a discrete configuration. The continuous configuration allows infinite degrees of freedom (DoFs) of the robots, which can adapt to the external environment during motion, but can hardly withstand large loads. Discrete configuration provides limited DoFs and controllable motion, mainly involving sliding joints [13], rolling joints [14, 15], and universal joints [16, 17]. Among these joints, rolling joints help avoid slack of the cables on both sides of the joint during the motion, which maintains the stability of snake-like robots and reduces the drive motors [18–20].

According to the matching between the actuation DoFs and joint DoFs, snake-like robots can be divided into underactuated systems and fully actuated systems. For underactuated systems, there are more joint DoFs than actuation DoFs [21–23]. In fact, excessive joint DoFs will reduce the system accuracy, although the control of end effector does not require the control of all joint DoFs [24]. Therefore, previous studies tried to predict the bending shape of underactuated robots for improving the accuracy [25–29]. Although these efforts contribute to achieving more accurate control [30–32], they are still faced with challenges of high control difficulty and poor load performance [33]. Different from underactuated systems, traditional fully actuated systems have equal joint DoFs and actuation DoFs, which inevitably increases the number of motors, increasing the difficulty of system control and the volume of

© The Author(s), 2025. Published by Cambridge University Press.

https://doi.org/10.1017/S0263574725102452 Published online by Cambridge University Press

the drive end. In many cases, redundant cables are employed to enhance system robustness and avoid the impact of cable wear and breakage [34, 35], which further increases the number of driving cables. The use of "layer-driven" method can partially alleviate this contradiction [36]. Still, cables driven by the same motor are distributed along a radial line, which limits the miniaturization of distal joints.

When the number of motors is less than the number of distal joints, there will be coupling between joints for realizing accurate motion control. Additionally, it is difficult to provide a constant curvature operating channel for snake-like robots in the complex and variable practical working environments, and joints in the same direction may have different rotation angles [37, 38]. Therefore, it is necessary to precisely drive the distal joints with fewer motors/DoFs, which helps eliminate the constraints on cable configuration in the distal joints and achieve a controllable rotation angle for each joint. This study adopts coordinate-based analysis to explore the transmission relationship of rolling joints, which describes the variation in the length of cables driving multiple pairs of rolling joints in any configuration. Further, a planar synergy drive system (PSDS) with a sphere-pin pair was proposed, and a prototype was built to verify its feasibility. Theoretical analysis reveals that the PSDS offers advantages of flexible cable configuration, which also supports variable curvature configurations of the distal joints.

The remainder of the paper is arranged as follows. Section 2 elaborates on the analysis of rolling joints and proposes the PSDS. In Section 3, a prototype of the PSDS is constructed and experimentally validated. Section 4 analyzes the experimental results to confirm the feasibility of the PSDS and theoretically validates its superiority over the capstan-driven systems. Finally, Section 5 provides a comprehensive summary of the entire paper.

2. Methods

2.1. Coordinate-based analysis of rolling joints

In this section, the structural characteristics of rolling joints are investigated, and coordinate-based analysis is adopted to describe the position of the cables, thus to analyze the relationship between the cable length variation (CLV) of rolling joints and the rotation angle of each joint. Specifically, the CLV is represented by a matrix.

The following assumptions are made for subsequent analysis:

1. The cables are flexible and inextensible.
2. The position of the cable remains relatively fixed along the distal joints, and the CLV is non-zero.
3. The rotation angle for each joint is non-zero, and the joints move through a pure rolling motion.

Figure 1 presents different states of the rolling joints. When a joint rotates by an angle θ, the CLV at a distance d from the neutral position is:

$$\Delta L = L_1' - L_1 = L_2 - L_2' = 2d \sin\frac{\theta}{2} \tag{1}$$

Let:

$$a = \frac{\Delta L}{d} = 2\sin\frac{\theta}{2} \tag{2}$$

where L_1, L_1', L_2, and L_2' represent the initial lengths and the lengths after rotation of the cables, respectively, and ΔL represents CLV. The a represents the variation in cable length per unit length at a distance from the neutral position.

Obviously, there is a one-to-one mapping relationship between a and θ. Therefore, we use a to replace θ in subsequent derivations to simplify algebraic operations.

Figure 1(c) and (d) illustrate a pair of rolling joints in the initial state and after rotation, respectively. A coordinate system is established on the base disk, as shown in Figure 1(e), where the x and y axes represent the projections of the two initial rotation axes. In this way, the position of all driving cables

https://doi.org/10.1017/S0263574725102452 Published online by Cambridge University Press

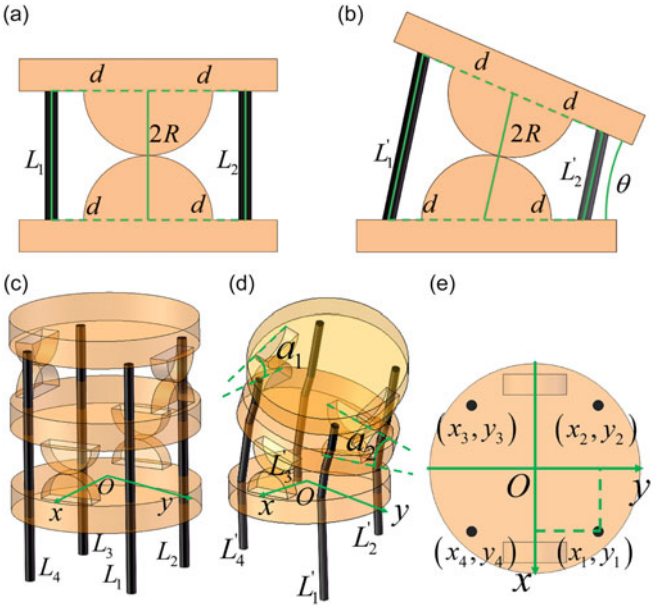


Figure 1. *Illustrations of the rolling joints. (a) Single joint before rotation; (b) Single joint after rotation; (c) A pair of rolling joints before rotation; (d) A pair of rolling joints after rotation; (e) The position of each cable expressed with coordinates.*

can be represented in specific. Here, we define that the shortening of the driving cable corresponds to a positive CLV under forward rotation of a rotation axis, and the CLV of the ith cable is:

$$\Delta L_i = a_1 x_i + a_2 y_i \tag{3}$$

The above equation elucidates the relationship between the CLV and the coordinates. Although we analyze the CLV using the positions of four cables here, this equation evidently holds true for cables at arbitrary positions.

Figure 2(a) shows the rotation of two pairs of rolling joints and coordinates of the driving cables, and we have:

$$\begin{cases} \Delta L_{1,i} = a_{1,1} x_{1,i} + a_{1,2} y_{1,i} \\ \Delta L_{2,i} = \sum_{k=1}^{2} a_{k,1} x_{2,i} + \sum_{k=1}^{2} a_{k,2} y_{2,i} \end{cases} \tag{4}$$

where $x_{i,j}$ and $y_{i,j}$ represent the horizontal axis and the vertical axis of the jth cable on the ith pair of rolling joints, respectively, and $a_{i,j}$ represents the rotation of the jth ($j = 1$ or 2) in the ith pair of joints.

Clearly, the above equation holds true for any number of pairs of rolling joints. For m pairs of rolling joints with n cables on each pair, as shown in Figure 2(b), the CLV of the jth cable on the ith pair of rolling joints is:

$$\Delta L_{i,j} = \sum_{k=1}^{i} \left(a_{k,1} x_{i,j} + a_{k,2} y_{i,j} \right) \tag{5}$$

Here, we can drive these rolling joints using two DoFs, causing coupling of all joints in each direction during rotation. Let:

$$\begin{cases} a_{1,1} : a_{2,1} : a_{3,1} \ldots : a_{m,1} = 1 : p_2 : p_3 : \ldots : p_m \\ a_{1,2} : a_{2,2} : a_{3,2} \ldots : a_{m,2} = 1 : q_2 : q_3 : \ldots : q_m \end{cases} \tag{6}$$

https://doi.org/10.1017/S0263574725102452 Published online by Cambridge University Press

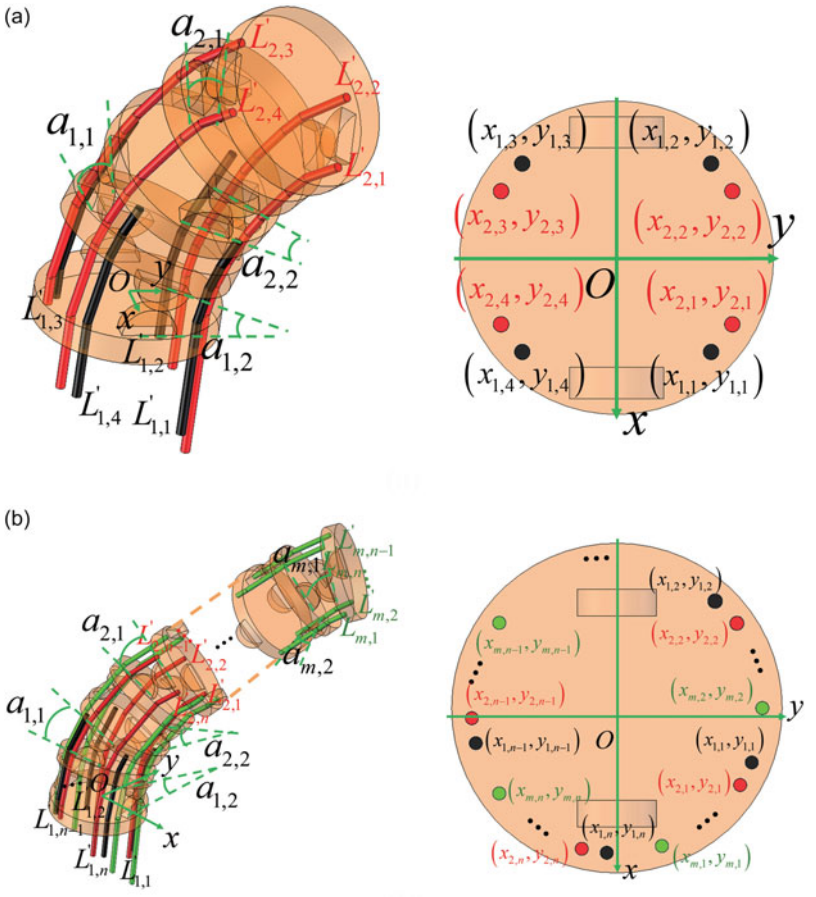


Figure 2. *Multiple pairs of rolling joints. (a) Rotation of two pairs of rolling joints and coordinates of the driving cables; (b) Rotation ofmpairs of rolling joints (withncables on each pair) and coordinates of the driving cables.*

Let $p_1 = q_1 = 1$ for convenience. In this way, we have:

$$\Delta L_{i,j} = \sum_{k=1}^{i} \left(p_k a_{1,1} x_{i,j} + q_k a_{1,2} y_{i,j} \right) \tag{7}$$

The matrix formed by the CLVs of all cables is:

$$L_{mat} = \begin{bmatrix} \Delta L_{1,1} & \Delta L_{1,2} & \dots & \Delta L_{1,n} \\ \Delta L_{2,1} & \Delta L_{2,2} & \dots & \Delta L_{2,n} \\ \dots & \dots & \dots & \dots \\ \Delta L_{m,1} & \Delta L_{m,2} & \dots & \Delta L_{m,n} \end{bmatrix} \tag{8}$$

2.2. The PSDS with a sphere-pin pair

To drive the multiple rolling joints, this section proposes a novel drive system with a sphere-pin pair, and the working principle is illustrated in Figure 3. Fork 2 of the sphere-pin pair can achieve two DoFs of rotation relative to Fork 1, and the center plane of the spider is taken as the initial plane (the original Fork 2 plane in Figure 3(a)). This plane turns to Fork 2 plane′ after rotation (Figure 3(b)). The rotation can be represented by two parameters, φ_1 and φ_2, corresponding to the rotation angles along two orthogonal

https://doi.org/10.1017/S0263574725102452 Published online by Cambridge University Press

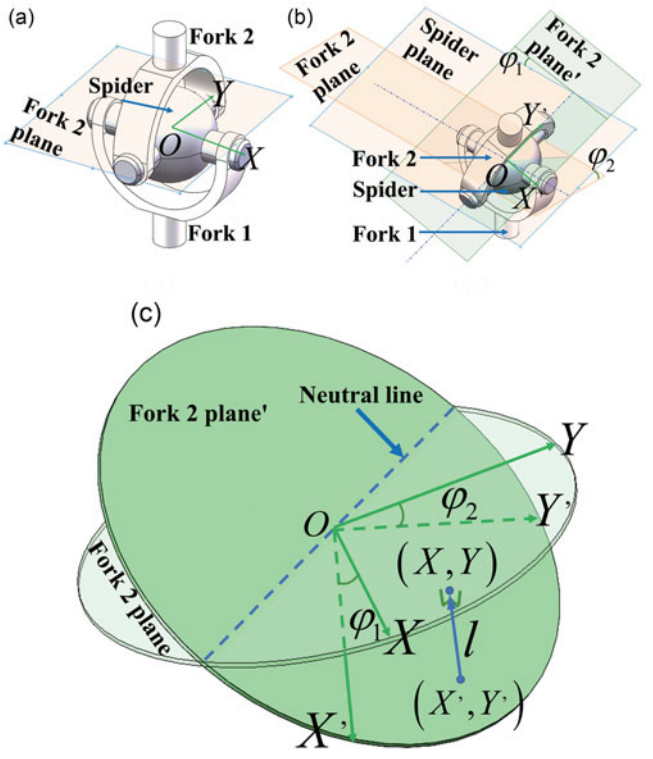


Figure 3. *The working principle of the PSDS. (a) Initial pose of the sphere-pin pair; (b) Pose of the sphere-pin pair after rotation; (c) The directed distance from Fork 2 plane′ to a point on Fork 2 plane.*

directions, respectively. Then, the directed distance l from Fork 2 plane′ to point (X, Y) on Fork 2 plane (Figure 3(c)) can be expressed as:

$$l = X \tan \varphi_1 + Y \tan \varphi_2 \tag{9}$$

Clearly, l is a linear combination of X and Y. Taking l as the model of drive value to drive the rolling joints, the following drive matrix L_{mat2} is obtained as:

$$L_{mat2} = \begin{bmatrix} l(X_{1,1}, Y_{1,1}) & l(X_{1,2}, Y_{1,2}) & \dots & l(X_{1,n}, Y_{1,n}) \\ l(X_{2,1}, Y_{2,1}) & l(X_{2,2}, Y_{2,2}) & \dots & l(X_{2,n}, Y_{2,n}) \\ \dots & \dots & \dots & \dots \\ l(X_{m,1}, Y_{m,1}) & l(X_{m,2}, Y_{m,2}) & \dots & l(X_{m,n}, Y_{m,n}) \end{bmatrix} \tag{10}$$

where $X_{i,j}$ and $Y_{i,j}$ are the coordinates at the drive end, corresponding to the jth cable of the ith pair of rolling joints.

Since the drive value is equal to the CLV and the cable is inextensible, we have:

$$L_{mat} = L_{mat2} \tag{11}$$

Let:

$$\begin{cases} X_{i,j} = \dfrac{x_{i,j}}{k_1} \displaystyle\sum_{k=1}^{i} p_k \\ Y_{i,j} = \dfrac{y_{i,j}}{k_2} \displaystyle\sum_{k=1}^{i} q_k \end{cases} \tag{12}$$

https://doi.org/10.1017/S0263574725102452 Published online by Cambridge University Press

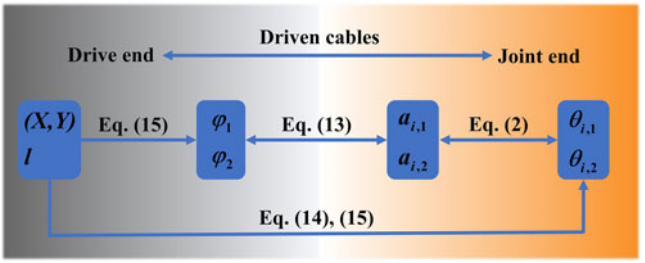


Figure 4. *Kinematic principle of the PSDS.*

where k_1 and k_2 represent customized non-zero positive proportional coefficients in two orthogonal directions at the drive end and joint end, and reducing k_1 and k_2 will result in a larger $a_{i,1}$ and $a_{i,2}$ for the same φ_1 and φ_2, and vise versa.

Eq. (12) provides the relationship between the drive end coordinates and the distal joint coordinates. Different operational scenarios require different rotation angles between the distal joints, that is, different configurations of p and q in Eq. (6). Since the derivation from Eq. (6) to Eq. (12) is reversible, Eq. (12) can be used to design the robot to meet specific practical requirements. Solving Eqs. (7), (8), (9), (10), (11) and (12) yields:

$$\begin{cases} a_{i,1} = p_i \dfrac{\tan \varphi_1}{k_1} \\ a_{i,2} = q_i \dfrac{\tan \varphi_2}{k_2} \end{cases} \tag{13}$$

If the position of the drive end is determined with Eq. (13), the angle of each distal joint will have a one-to-one mapping relationship with φ_1 and φ_2. For any non-zero drive value l at an arbitrary position (X, Y) at the drive end, we can obtain $\theta_{i,1}$, $\theta_{i,2}$, φ_1 and φ_2 with the trihedral angle cosine theorem as Eq. (14) and Eq. (15):

$$\begin{cases} \theta_{i,1} = 2 \arcsin \dfrac{p_i \tan \varphi_1}{2k_1} \\ \theta_{i,2} = 2 \arcsin \dfrac{q_i \tan \varphi_2}{2k_2} \end{cases} \tag{14}$$

$$\begin{cases} \varphi_1 = \begin{cases} \dfrac{Xl}{|Xl|} \arccos \left(\dfrac{X^2}{X^2+Y^2} \dfrac{\sqrt{X^2+Y^2}}{\sqrt{l^2+X^2+Y^2}} + \dfrac{Y^2}{X^2+Y^2} \right), X \neq 0 \\ 0, X = 0 \end{cases} \\ \varphi_2 = \begin{cases} \dfrac{Yl}{|Yl|} \arccos \left(\dfrac{Y^2}{X^2+Y^2} \dfrac{\sqrt{X^2+Y^2}}{\sqrt{l^2+X^2+Y^2}} + \dfrac{X^2}{X^2+Y^2} \right), Y \neq 0 \\ 0, Y = 0 \end{cases} \end{cases} \tag{15}$$

The mapping principle among the kinematic parameters of the PSDS is illustrated in Figure 4. It is worth noting that different combinations of (X, Y) and l can achieve the same effect, as long as X and Y correspond to the same radial line.

3. Experiment

3.1. Prototype design

A prototype was established based on the PSDS, which consisted primarily of a distal joint module, a cable guide module, and a drive module, as shown in Figure 5. The distal joint module had three pairs of rolling joints, each driven by five cables arranged uniformly circumferentially. The cable configuration

https://doi.org/10.1017/S0263574725102452 Published online by Cambridge University Press

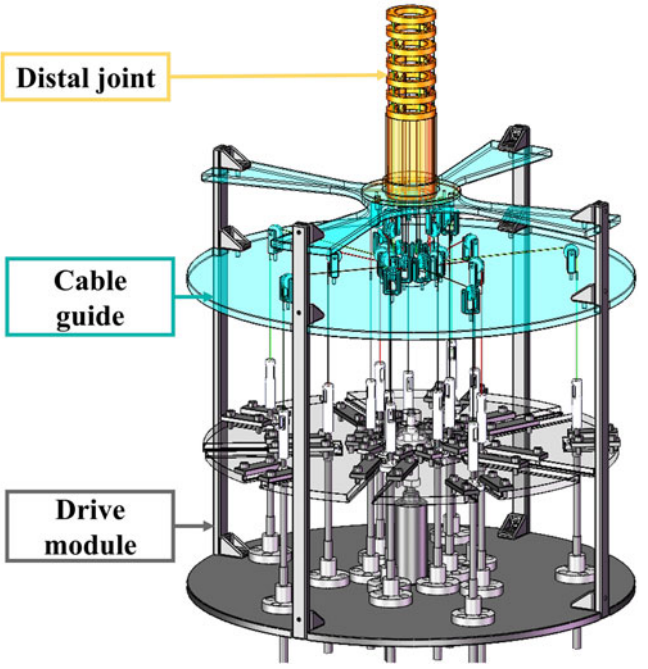


Figure 5. *Structure of the prototype.*

of the prototype is illustrated in Figure 6, and the cables for the three pairs of rolling joints are marked in black, red, and green, respectively.

For each cable, its position at both joint end and drive end lies on the same radial line. The relevant parameters are shown as Eq. (16):

$$\begin{cases} a_{1,1} : a_{2,1} : a_{3,1} = 1 : 1 : 2 \\ a_{1,2} : a_{2,2} : a_{3,2} = 1 : 1 : 2 \\ k_1 = k_2 = 0.5 \end{cases} \tag{16}$$

According to Eq. (12), we can obtain:

$$\begin{cases} (X_{1,k}, Y_{1,k}) = 2(x_{1,k}, y_{1,k}) \\ (X_{2,k}, Y_{2,k}) = 4(x_{2,k}, y_{2,k}) \\ (X_{3,k}, Y_{3,k}) = 8(x_{3,k}, y_{3,k}) \end{cases} \tag{17}$$

Specifically, the cross-sectional radius of the distal joints was 15 mm, and all cables were located on a circumference with a radius of 12.5 mm. The gear-shaped rolling joints were used to ensure the pure rolling between joints. The cables for the three pairs of rolling joints at the drive end were located on the circumferences with the radius of 25, 50, and 100 mm, respectively, so that Eq. (17) was satisfied.

Figure 6(a) shows the frame coordinate system of the distal joints, where the Y-axis can be determined using the right-hand rule. The joint thickness was $\delta = 4$ mm, and the radius of the rolling circle was $r =$ 3 mm. The maximum rotation angle of a single joint was 22.6°. For convenience, the rotation of a joint was equivalently represented as two rotations in the same direction, each with half the initial angle. The transformation matrix is expressed as follows:

$$T_i^{i-1} = \begin{bmatrix} \cos\theta_i & -\sin\theta_i & 0 & a_{i-1} \\ \sin\theta_i \cos\alpha_{i-1} & \cos\theta_i \cos\alpha_{i-1} & -\sin\alpha_{i-1} & -d_i \sin\alpha_{i-1} \\ \sin\theta_i \sin\alpha_{i-1} & \cos\theta_i \sin\alpha_{i-1} & \cos\alpha_{i-1} & d_i \cos\alpha_{i-1} \\ 0 & 0 & 0 & 1 \end{bmatrix} \tag{18}$$

https://doi.org/10.1017/S0263574725102452 Published online by Cambridge University Press

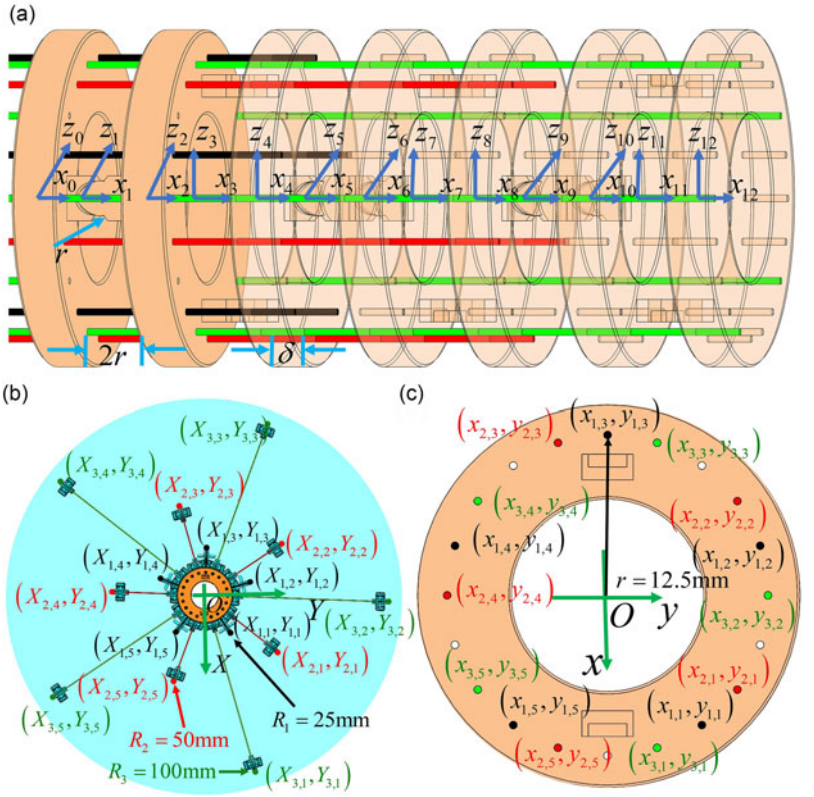


Figure 6. *Cable configuration for the prototype. (a) Overview of the distal joints, with the black, red, and green cables driving the first, second, and third pairs, respectively; (b) Cable configuration at the drive end; (c) Cable configuration at the joint end, with each cable's position at the drive end and joint end lying on the same radial line.*

The transformation matrix between the end effector coordinate system and the base coordinate system can be expressed as:

$$T_0^{12} = \prod_{i=1}^{12} T_i^{i-1} = \begin{bmatrix} \mathbf{R} & \mathbf{p} \\ 0 & 1 \end{bmatrix} \tag{19}$$

where **R** and **p** represent the orientation and position of the end effector relative to the base, respectively.

Based on this, the workspace of the end effector can be obtained, as shown in Figure 7.

The structural diagram of the drive module is shown in Figure 8. Fifteen drive units were assembled on the drive platform, which was connected to the center radial ball bearing. Each drive unit consisted of a tension rod, a radial ball bearing, and a push-pull rod. The thread coupling between the tension rod and the push-pull rod achieved the pretension of the cable. The design of the stepped shaft at the push-pull rod and nut allowed the push-pull rod to rigidly connect to the inner race of the radial ball bearing, while the outer race of the radial ball bearing could slide radially. The DoFs of the drive platform were limited to the rotation in two directions, since the rotation along the axial direction was restricted. The center axes of all radial ball bearings were constrained to the same plane as the center radial ball bearing to ensure the accuracy of the model. The schematic of the drive mechanism is illustrated in Figure 8(c).

https://doi.org/10.1017/S0263574725102452 Published online by Cambridge University Press

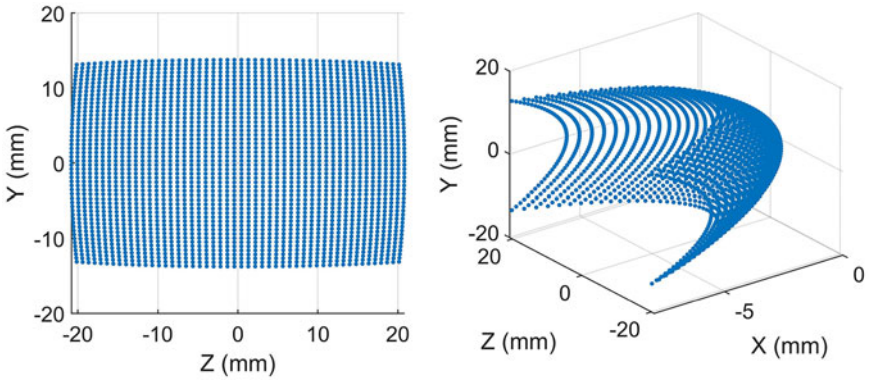


Figure 7. *The Y-Z view and 3-D view of the workspace.*

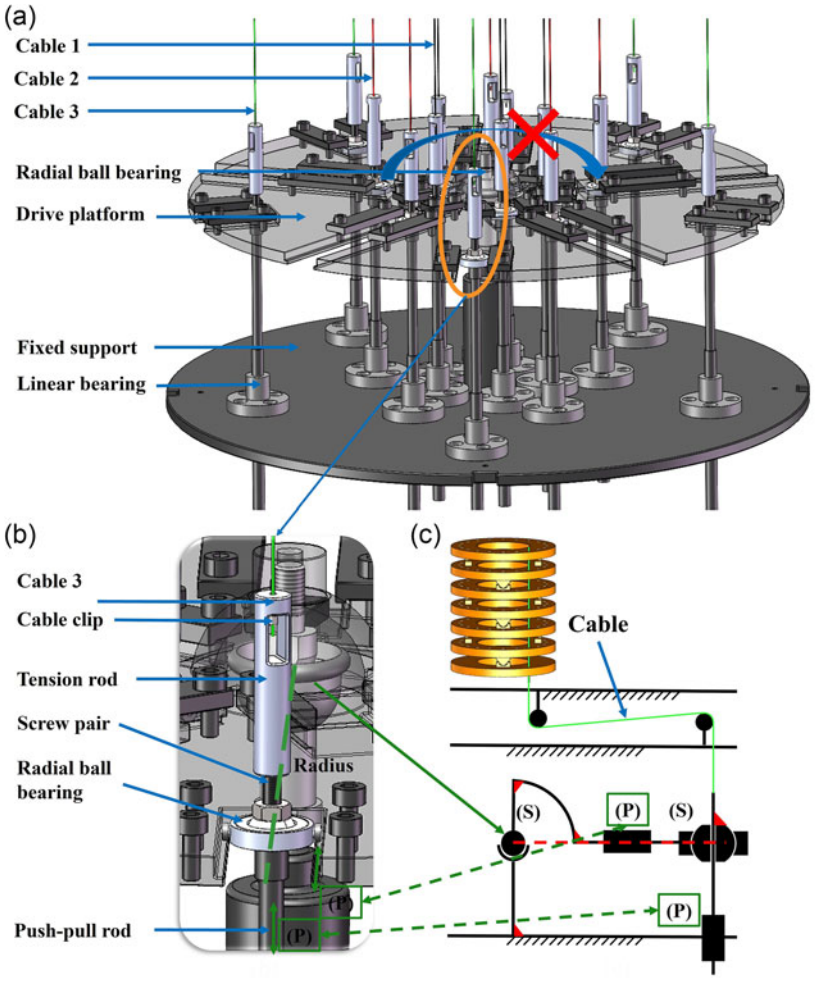


Figure 8. *Structural diagram of the drive module. (a) Overall structure, including 15 drive units and the drive platform; (b) A drive unit, capable of tensioning and driving the corresponding cable; (c) Schematic diagram of the drive system. (For illustrative purposes, the translational DoF of the radial joint bearing on the drive unit is slightly shifted from its actual position).*

https://doi.org/10.1017/S0263574725102452 Published online by Cambridge University Press

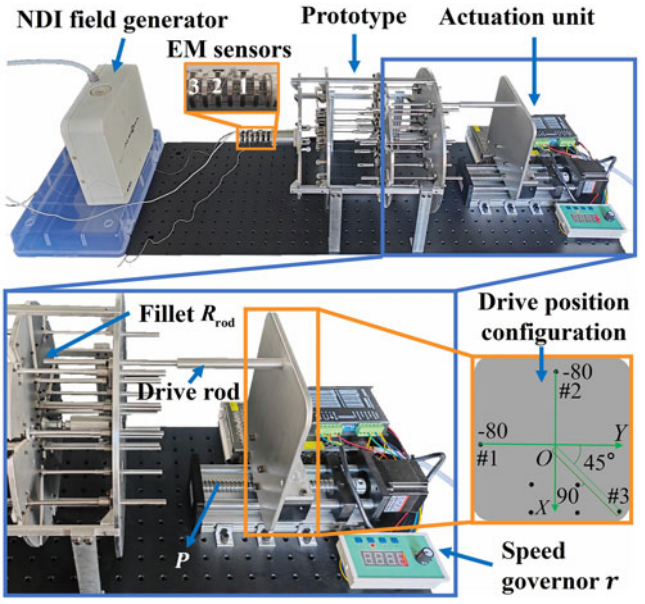


Figure 9. *Experimental setup, including NDI field generator, EM sensors, prototype system, and actuation unit.*

3.2. Experiment design

The overall experimental setup is shown in Figure 9. An EM sensor was fixed to the distal disk of each pair of rolling joints. The changes in the motion posture of the sensors relative to their initial postures were recorded to monitor the angular variation of each pair. The rotation of the distal joints was realized by pushing the drive platform with the drive rod. The three drive positions corresponding to coordinates $(-80, 0)$, $(0, -80)$, and $(45\sqrt{2}, 45\sqrt{2})$ (corresponding to experiment #1, #2 and #3, respectively) were selected to validate the drive scenarios in different directions. The first two experiments could only cause rotation in one direction (single-direction rotation group), while the third experiment could result in rotation in two directions (tilt group). The relationship between the drive value l and the time t could be obtained:

$$\begin{cases} \alpha = \arcsin \dfrac{R_{rod}}{\sqrt{X^2 + Y^2 + (rPt - R_{rod})^2}} \\ \beta = \arcsin \dfrac{rPt - R_{rod}}{\sqrt{X^2 + Y^2 + (rPt - R_{rod})^2}} \\ l = \sqrt{X^2 + Y^2} \tan(\alpha + \beta) \end{cases} \tag{20}$$

where $R_{rod} = 2.5$ mm, $r = 1$ r/min, and $P = 5$ mm, represented the end fillet radius of the drive rod, the rotation speed of the governor, and the pitch of the lead screw, respectively.

4. Results and discussion

The results of the three sets of experiments are shown in Figure 10. The mean absolute error (MAE) and root mean square error (RMSE) were used to reflect the accuracy of the prototype.

4.1. Motion characteristics of distal joints

The motion performance of the distal joints was tested to characterize the performance of the PSDS. Due to the highly nonlinear relationship between parameter a and the rotation angle of the sensors in the

https://doi.org/10.1017/S0263574725102452 Published online by Cambridge University Press

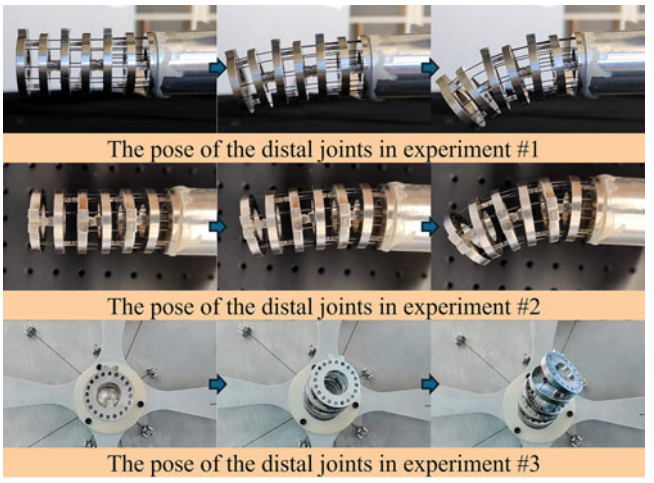


Figure 10. *The pose of the distal joints in the experiments.*

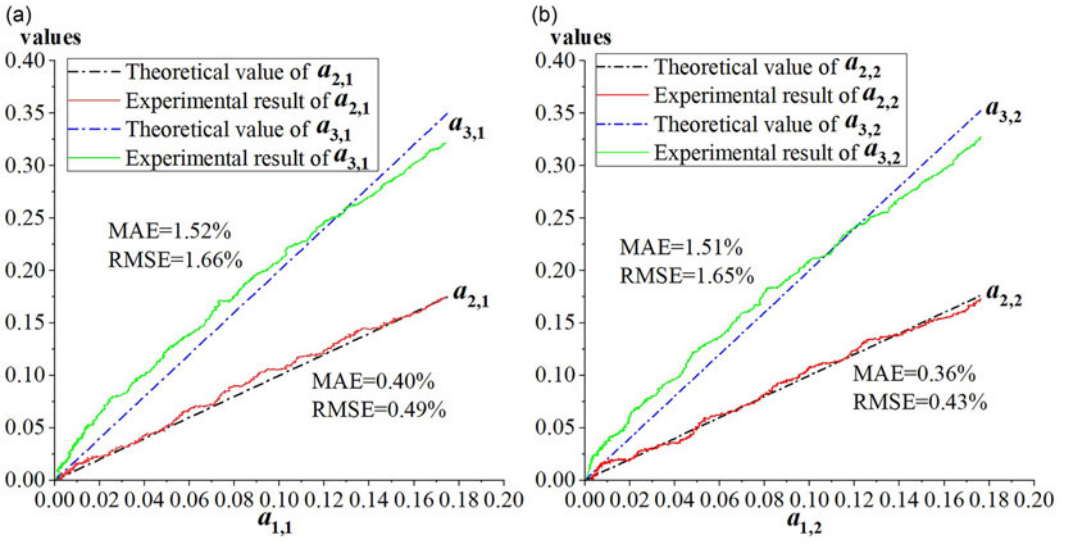


Figure 11. *The parameter a of the distal joints in (a) experiment #1 and (b) experiment #2.*

tilt group, the verification was carried out with single-direction rotation group. In the single-direction rotation group, each parameter *a* of the three pairs of rolling joints was calculated based on the rotation angles of the distal joints. The rotation angle of each distal joint was calculated from the rotation angles of the EM sensor's axis. The rotation angle of the first pair of joints was the rotation angle of EM sensor 1, the second pair's rotation angle was the difference between the rotation angles of EM sensors 2 and 1, and the third pair's rotation angle was the difference between the rotation angles of EM sensors 3 and 2. The error in this analysis was defined as the error of distal joint precision. The experimental results are shown in Figure 11 (the horizontal axes reflecting the actual rotation angle of the first joint pair and the vertical axes reflecting the theoretical and measured rotation angles of the second and third joints).

4.2. Accuracy of the driving model

The measured rotation angles of the distal joints were compared with the theoretical rotation angles, and the theoretical rotation angles could be obtained from Eqs. (14), (15) and (20). For experiment #1

https://doi.org/10.1017/S0263574725102452 Published online by Cambridge University Press

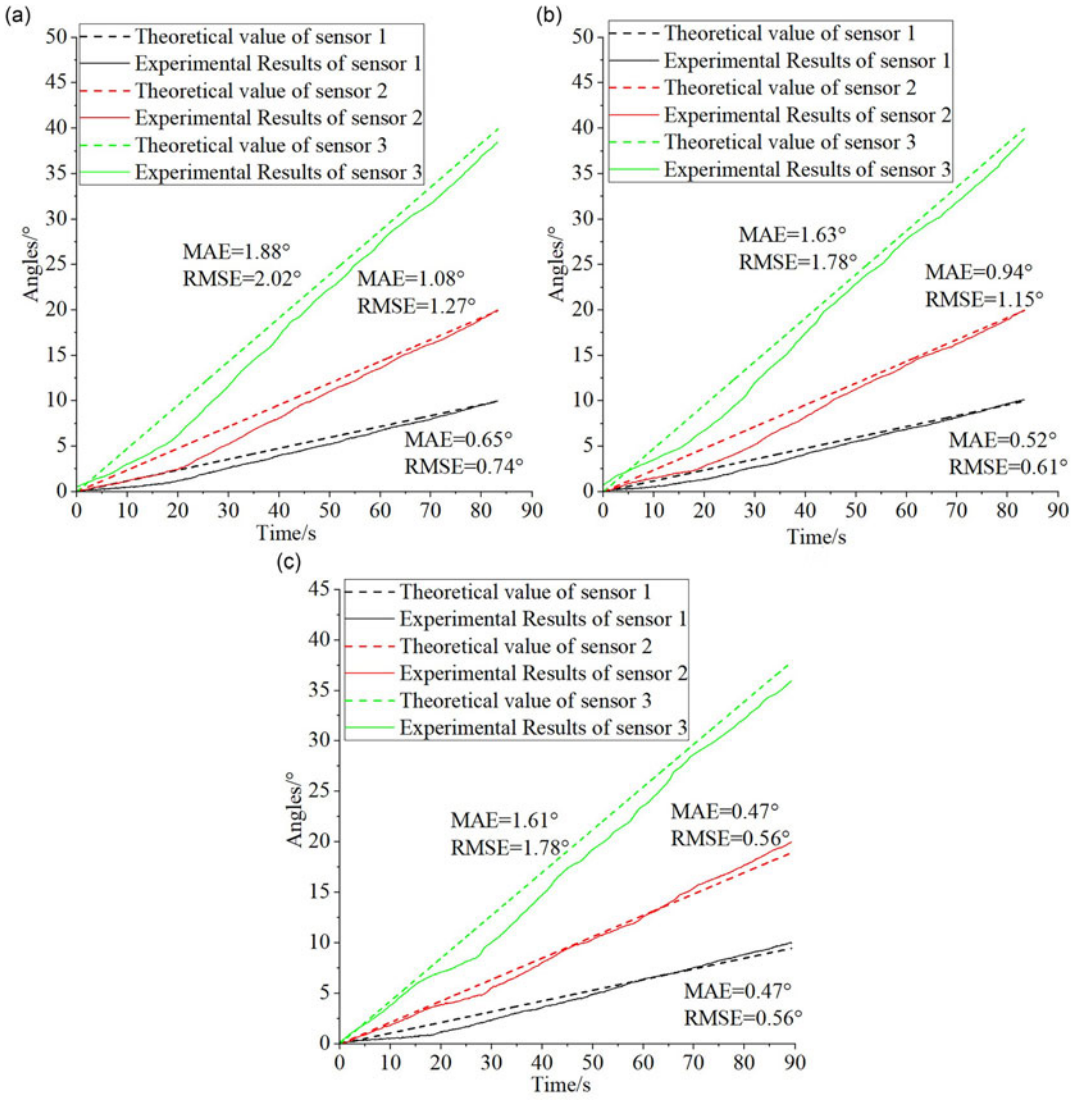


Figure 12. *Experimental and theoretical rotation angles of the distal joints in (a) experiment #1, (b) experiment #2 and (c) experiment #3.*

and experiment #2 (the single-direction rotation group), the theoretical angle of each sensor could be directly obtained through the rotation angle θ of the joint. However, in experiment #3 (the tilt group), we needed to calculate the theoretical rotation angles of all joints, and then obtain the rotation matrices of all joints relative to the fixed disk at the base. Finally, the theoretical rotation angles of all sensors were obtained from the rotation matrices. The error in this analysis was defined as the error of the driving model precision. The experimental results are shown in Figure 12 (the horizontal axes reflecting time t and the vertical axes reflecting the theoretical and measured rotation angles of the three joint pairs at the end effector).

4.3. Discussion

In the experiment, a relatively low speed of the actuation unit was set to assist the observation of the experimental results and approximate a quasi-static experimental process. During the experiment, the

https://doi.org/10.1017/S0263574725102452 Published online by Cambridge University Press

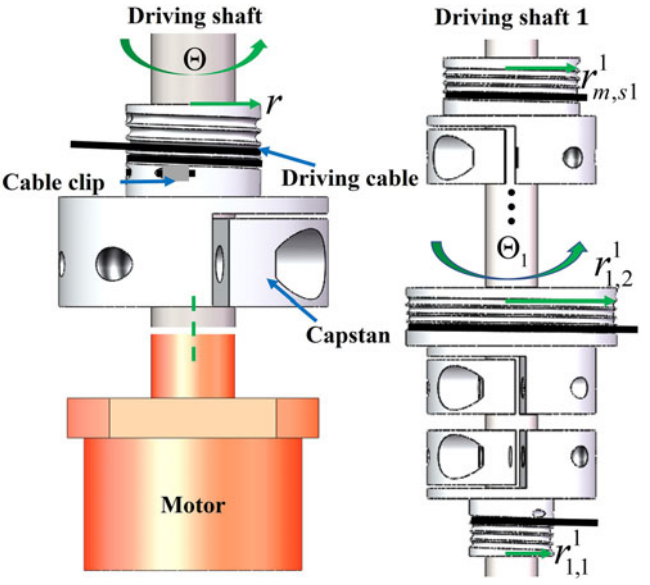


Figure 13. *Capstan connected to motor output shaft for cable wrapping.*

motion of the drive platform was not smooth but showed slight lags, although the output of the drive unit was uniform and linear. The drive rod might tilt when the drive platform moved to positions with high resistance, making the actual rotation angle of the distal joint slightly lower than the theoretical angle. However, the tilt of the drive rod got relieved along with a gradual decrease in the resistance, and the measured values gradually approached the theoretical values. In the analysis of the accuracy of joint rotation angles, the rotation of the first and second pairs of rolling joints met expectations, while there were some errors in the rotation of the third pair. This may be related to processing errors on the mating surface and tooth profile in the third pair.

Driving a pair of rolling joints typically requires either three or four driving cables. However, any slackness or failure of a cable can lead to loss of control over the joint's movement. In our prototype, we use five driving cables to control each pair of distal joints, ensuring that the prototype can still operate normally even if one cable becomes slackened or broken, thus improving operational safety and load capacity. This also shows an advantage of the PSDS: allowing for an increase in the number of driving cables without adding extra DoFs. It is important to note that the initial assembly of the prototype becomes increasingly difficult as the number of driving cables increases. It is challenging to ensure that all cables maintain the same pretension forces while keeping the distal joints in their initial posture. Additionally, as the number of tests increases, the cables will inevitably experience wear and irreversible elongation. As a result, a small number of driving cables may become slackened during the experiments.

Overall, the errors in the experiments were mainly related to the machining precision and assembly precision. The maximum MAE of the distal joint precision and the driving model precision was 1.52% and 1.88°, respectively, and the maximum RMSE was 1.66% and 2.02°, respectively. This result essentially verifies the accuracy of the PSDS.

Next, we will further quantify the advantages of the PSDS through the comparison with the capstan-driven approaches. Figure 13 illustrates the working principle of the capstan-driven approach, where one motor shaft can be connected to multiple capstans. For each capstan, the drive value l' is:

$$l' = r\Theta \tag{21}$$

where r is the radius of the capstan and Θ is the rotation angle of the motor output shaft.

The capstans driven by the same motor share the same Θ. Two motors are adopted to drive the distal joints to compare with the PSDS. Assuming that the number of cables driven by the two motors in each

https://doi.org/10.1017/S0263574725102452 Published online by Cambridge University Press

pair of joints is s_1 and s_2 respectively, the drive matrix L'_{mat2} can be obtained:

$$L'_{mat2} = \begin{bmatrix} \Theta_1 r^1_{1,1} & \Theta_1 r^1_{1,2} & \dots & \Theta_1 r^1_{1,s_1} & \Theta_2 r^2_{1,1} & \Theta_2 r^2_{1,2} & \dots & \Theta_2 r^2_{1,s_2} \\ \Theta_1 r^1_{2,1} & \Theta_1 r^1_{2,2} & \dots & \Theta_1 r^1_{2,s_1} & \Theta_2 r^2_{2,1} & \Theta_2 r^2_{2,2} & \dots & \Theta_2 r^2_{2,s_2} \\ \dots & \dots & \dots & \dots & \dots & \dots & \dots & \dots \\ \Theta_1 r^1_{m,1} & \Theta_1 r^1_{m,2} & \dots & \Theta_1 r^1_{m,s_1} & \Theta_2 r^2_{m,1} & \Theta_2 r^2_{m,2} & \dots & \Theta_2 r^2_{m,s_2} \end{bmatrix} \tag{22}$$

where $r^i_{j,k}$ represents the radius of the capstan corresponding to the kth cable of the jth pair of joints driven by the ith motor.

Drive the joints with this approach, and we have:

$$L_{mat} = L'_{mat2} \tag{23}$$

First, examine each row of the Eq. (23), which represents the drive values and CLVs of the multiple cables driven by the same motor in each pair of rolling joints. Taking the first row as an example:

$$\begin{bmatrix} a_{1,1} \\ a_{1,2} \end{bmatrix}^{\mathsf{T}} \begin{bmatrix} x_{1,1} & y_{1,1} \\ x_{1,2} & y_{1,2} \\ \dots & \dots \\ x_{1,s_1} & y_{1,s_1} \end{bmatrix}^{\mathsf{T}} = \Theta_1 \begin{bmatrix} r^1_{1,1} \\ r^1_{1,2} \\ \dots \\ r^1_{1,s_1} \end{bmatrix}^{\mathsf{T}} \tag{24}$$

Therefore:

$$\begin{bmatrix} a_{1,1} \\ a_{1,2} \end{bmatrix}^{\mathsf{T}} \begin{bmatrix} x_{1,1}\dfrac{r^1_{1,s_1}}{r^1_{1,1}} & y_{1,1}\dfrac{r^1_{1,s_1}}{r^1_{1,1}} \\ x_{1,2}\dfrac{r^1_{1,s_1}}{r^1_{1,2}} & y_{1,2}\dfrac{r^1_{1,s_1}}{r^1_{1,2}} \\ \dots \quad \dots & \\ x_{1,s_1} & y_{1,s_1} \end{bmatrix}^{\mathsf{T}} = \Theta_1 r^1_{1,s_1} \begin{bmatrix} 1 \\ 1 \\ \dots \\ 1 \end{bmatrix}^{\mathsf{T}} \tag{25}$$

Note that $a_{1,1}$ and $a_{1,2}$ are independent of each other. Assuming each x is non-zero, we have:

$$\frac{y_{1,1}}{x_{1,1}} = \frac{y_{1,2}}{x_{1,2}} = \dots = \frac{y_{1,s_1}}{x_{1,s_1}} \tag{26}$$

The above equation means that the coordinates $(x_{1,1}, y_{1,1})$, …, (x_{1,s_1}, y_{1,s_1}) all lie on a line passing through the origin (**Conclusion 1**).

Next, analyze each column, which represents the CLVs and drive values of a motor in different joints. Taking the first column as an example, we can obtain:

$$\begin{bmatrix} a_{1,1} \\ a_{1,2} \end{bmatrix}^{\mathsf{T}} \begin{bmatrix} x_{1,1} & y_{1,1} \\ (p_1+p_2)x_{2,1} & (q_1+q_2)y_{2,1} \\ \dots & \dots \\ \left(\sum_{k=1}^{m} p_m\right) x_{m,1} & \left(\sum_{k=1}^{m} q_m\right) y_{m,1} \end{bmatrix}^{\mathsf{T}} = \Theta_1 \begin{bmatrix} r^1_{1,1} \\ r^1_{2,1} \\ \dots \\ r^1_{m,1} \end{bmatrix}^{\mathsf{T}} \tag{27}$$

Therefore:

$$\begin{bmatrix} a_{1,1} \\ a_{1,2} \end{bmatrix}^{\mathsf{T}} \begin{bmatrix} x_{1,1}\dfrac{r^1_{m,1}}{r^1_{1,1}} & y_{1,1}\dfrac{r^1_{m,1}}{r^1_{1,1}} \\ (p_1+p_2)x_{2,1}\dfrac{r^1_{m,1}}{r^1_{2,1}} & (q_1+q_2)y_{2,1}\dfrac{r^1_{m,1}}{r^1_{2,1}} \\ \dots \quad \dots & \\ \left(\sum_{k=1}^{m} p_m\right) x_{m,1} & \left(\sum_{k=1}^{m} q_m\right) y_{m,1} \end{bmatrix}^{\mathsf{T}} = \Theta_1 r^1_{m,1} \begin{bmatrix} 1 \\ 1 \\ \dots \\ 1 \end{bmatrix}^{\mathsf{T}} \tag{28}$$

https://doi.org/10.1017/S0263574725102452 Published online by Cambridge University Press

Since $a_{1,1}$ and $a_{1,2}$ are independent of each other, the coefficients on the left side of the equation must be equal:

$$\begin{cases} x_{1,1}\dfrac{r^1_{m,1}}{r^1_{1,1}} = (p_1+p_2)x_{2,1}\dfrac{r^1_{m,1}}{r^1_{2,1}} \\ x_{1,1}\dfrac{r^1_{m,1}}{r^1_{1,1}} = (p_1+p_2+p_3)x_{3,1}\dfrac{r^1_{m,1}}{r^1_{3,1}} \\ \cdots \\ x_{1,1}\dfrac{r^1_{m,1}}{r^1_{1,1}} = \left(\sum_{k=1}^{m} p_m\right)x_{m,1} \end{cases} \tag{29a}$$

$$\begin{cases} y_{1,1}\dfrac{r^1_{m,1}}{r^1_{1,1}} = (q_1+q_2)y_{2,1}\dfrac{r^1_{m,1}}{r^1_{2,1}} \\ y_{1,1}\dfrac{r^1_{m,1}}{r^1_{1,1}} = (q_1+q_2+q_3)y_{3,1}\dfrac{r^1_{m,1}}{r^1_{3,1}} \\ \cdots \\ y_{1,1}\dfrac{r^1_{m,1}}{r^1_{1,1}} = \left(\sum_{k=1}^{m} q_m\right)y_{m,1} \end{cases} \tag{29b}$$

Therefore:

$$\frac{y_{1,1}}{x_{1,1}} = \frac{(q_1+q_2)y_{2,1}}{(p_1+p_2)x_{2,1}} = \ldots = \frac{\left(\sum_{k=1}^{m} q_m\right)y_{m,1}}{\left(\sum_{k=1}^{m} p_m\right)x_{m,1}} \tag{30}$$

According to the above equation, the position of the cables is constrained by the configuration of p and q. In practical engineering, a constant curvature model is usually used to illustrate the motion of snake-like joints, which requires the rotation angles of codirectional joints to be the same, meaning that all cables shall be on the same diameter line (The Eq. (30) will degenerate into Eq. (26)). Combining **Conclusion 1**, it can be inferred that all cables driven by the same motor are aligned on the same line. As the number of joints increases, this leads to an significant increase in the cross-sectional area of distal joints, restricting the use of snake-like robots in the scenarios involving limited space, such as minimally invasive surgery.

Figure 14 illustrates two capstan-driven approaches that achieve the same effect as the proposed prototype. According to Figure 14, it can be found that using the capstan-driven approach will undoubtedly result in greater cross-sectional space occupancy or more drive motors. Assuming that the diameter of the cable channel is d_c, the radius of the internal working channel of the joint is r_0, the minimum wall thickness of the solid structure is δ, and there are n pairs of rolling joints, as shown in Figure 15. Then, the radius r_c of distal joint for the capstan-driven approach and the radius r_p of distal joints for the PSDS are:

$$\begin{cases} r_c = r_0 + nd_c + (n+1)\delta \\ r_p = r_0 + d_c + 2\delta \end{cases} \tag{31}$$

The additional joint cross-sectional area occupied by the driving cable in capstan-driven approach and the PSDS are s_c and s_p, respectively:

$$\begin{cases} s_c = \pi r_c^2 - \pi(r_0+\delta)^2 \\ s_p = \pi r_p^2 - \pi(r_0+\delta)^2 \end{cases} \tag{32}$$

https://doi.org/10.1017/S0263574725102452 Published online by Cambridge University Press

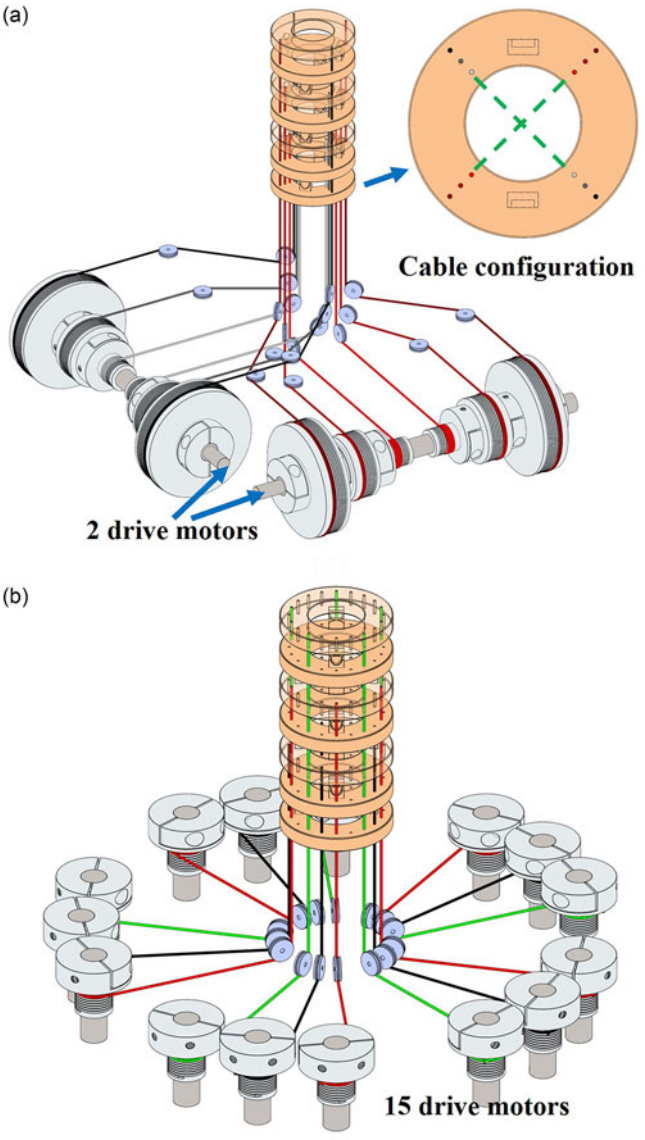


Figure 14. *Capstan-driven approaches to achieve the same effect as the PSDS. (a) Approach of using fewer motors; (b) Approach of using more motors.*

Compared with the capstan-driven approach, the PSDS shows smaller joint cross-sectional area, and the reduction ratio s_r is:

$$s_r = \frac{s_c - s_p}{s_c} = 1 - \frac{2r_0 + d_c + 3\delta}{2nr_0 + n^2 d_c + n(n+2)\delta} \tag{33}$$

As revealed in Eq. (33), a greater number of n indicates more pronounced advantage of PSDS over the capstan-driven approach.

When the capstan-driven system has the same end cable configuration as the PSDS, the required number of motors m_c is the number of non-collinear cables in all cable channels, whereas the PSDS only requires two drive motors. Therefore, the reduction rate of drive motors m_r is:

$$m_r = \frac{m_c - 2}{m_c} \tag{34}$$

https://doi.org/10.1017/S0263574725102452 Published online by Cambridge University Press

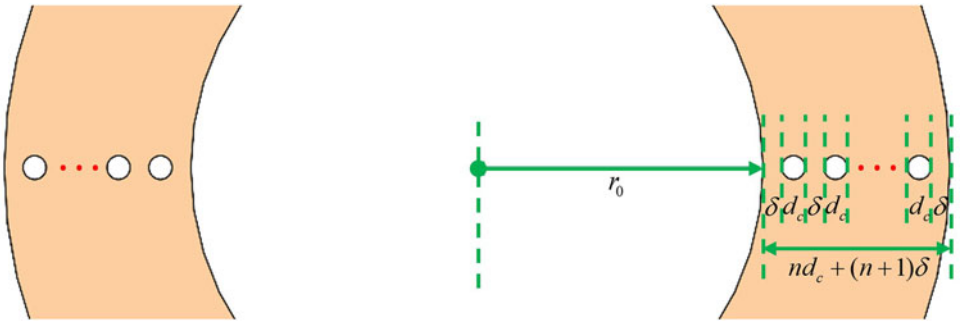


Figure 15. *Cross-sectional configuration of the distal joint under the Capstan-driven approach with two drive motors.*

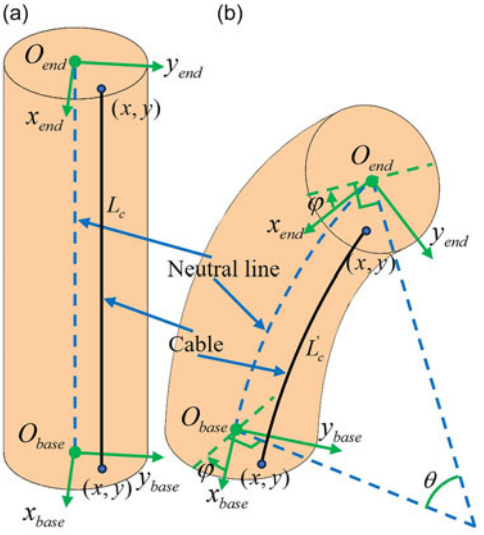


Figure 16. *Structure of the continuum joint applicable to the PSDS: (a) initial state and (b) bending state.*

In brief, a larger number of non-collinear cables results in more pronounced advantage of the PSDS over the capstan-driven approach. Eqs. (33) and (34) quantify the advantages of PSDS in terms of cross-sectional area occupation and the number of drive motors.

The core of the PSDS lies in that l is a linear combination of the coordinates X and Y. Therefore, the PSDS can drive the distal joints as long as the CLVs of the cables can be achieved by linearly adding the two orthogonal directions x and y. In this way, the continuum joint can be directly driven by the PSDS (based on the constant curvature model), as shown in Figure 16, with $L_c' - L_c = -x\theta \sin\varphi - y\theta \cos\varphi$. Similarly, the dual continuum-driven approach can also enhance load capacity and operational safety through the coordination of multiple cables, which operate the end continuum by controlling the proximal continuum (as referenced in ref. [39]). However, the curvature of the end continuum remains constant throughout. In contrast, the PSDS can achieve different segmented curvatures at the end by adjusting the configuration of p and q in Eq. (6), making it more adaptable to the complex and dynamic operational environments. Additionally, the cable shall remain relatively fixed along the position of the distal joints, and cable layouts with special configurations [40] are not suitable for the PSDS.

Overall, the PSDS offers the following advantages over the capstan-driven system:

https://doi.org/10.1017/S0263574725102452 Published online by Cambridge University Press

1. More flexible cable configuration: The PSDS allows for a more flexible cable configuration, which efficiently utilizes the available space at the distal joints to reduce the size. This is particularly meaningful for applications with size constraints, such as minimally invasive surgery.
2. More accurate driving model: The driving model is more accurate, with simplified kinematics. It enables precise control of the rotation angle of each joint without increasing the drive DoFs.

It is worth noting that PSDS can only ensure precise drive of the distal joints under the assumption that the cables are inextensible. In practice, when the joints bend significantly from its initial position, the cable can move and witness accumulated wear, which may lead to irreversible elongation of the cables, thus affecting the accuracy of PSDS.

5. Conclusion

In this paper, a novel PSDS is proposed. Compared with the capstan-driven system, the PSDS can significantly reduce the constraints on the configuration of cables, which brings several benefits, including further reduction in the size of the distal joints, a more accurate driving model, and easier implementation of variable curvature configuration. These advantages make the PSDS more suitable for applications in spatially constrained scenarios such as minimally invasive surgery. This study analyzed the matrix between the distal joints and drive system with a coordinate-based method, proposing two quantifiable parameters to demonstrate the advantages of the PSDS. The correctness and superiority of the driving model were verified through the experiment with a prototype, and the maximum MAE of the distal joint precision and the driving model precision was 1.52% and 1.88°, respectively.

The prototype used in the experiment of this paper suffers from the large size of the drive module and the difficulty of assembly. In the future, more optimal mechanical systems based on the PSDS model will be investigated.

Financial support. This work was supported by the National Key Research and Development Program of China. Grant No. 2022YFB4700801. This work was also supported by the Emerging Frontiers Cultivation Program of Tianjin University Interdisciplinary Center.

Competing interests. The authors declare that they have no known competing financial interests or personal relationships that could have appeared to influence the work reported in this paper.

Ethics approval and consent to participate. This article does not contain any studies with human participants or animals performed by any of the authors.

Consent for publication. All contributors agreed and given consent to publication.

Availability of data and material. Data that has been used is confidential.

References

[1] V. Vitiello, S. Lee, T. P. Cundy and G. Yang, "Emerging robotic platforms for minimally invasive surgery," *IEEE Rev. Biomed. Eng.* **6**, 111–126 (2012).
[2] Y. Zou, K. Pan, M. Wang, X. Lai, T. Lan, Z. Zhou and C. Li, "Accurate kinematic and stiffness analysis of parallel cable-driven upper limb rehabilitation robot with spherical guide wheel cable-guiding mechanism," *Robotica* **43**(3), 793–815 (2025).
[3] J. Chen, J. Yang, F. Qian, Q. Lu, Y. Guo, Z. Sun and C. Chen, "A novel inchworm-inspired soft robotic colonoscope based on a rubber bellows," *Micromachines-BASEL* **13**(4), 635 (2022).
[4] J. Li, Y. Zhao, Q. Tang, W. Sun, F. Yuan and X. Lu, "Conceptual design and error analysis of a cable-driven parallel robot," *Robotica* **40**(7), 2152–2167 (2022).
[5] Z. Ping, T. Zhang, C. Zhang, J. Liu and S. Zuo, "Design of contact-aided compliant flexure hinge mechanism using superelastic nitinol," *J. Mech. Des.* **143**(11), 114501 (2021).

https://doi.org/10.1017/S0263574725102452 Published online by Cambridge University Press

[6] C. He, S. Wang, Y. Xing and X. Wang, "Kinematics analysis of the coupled tendon-driven robot based on the product-of-exponentials formula," *Mech. Mach. Theory* **60**, 90–111 (2013).

[7] P. Racioppo and P. Ben-Tzvi, "Design and control of a cable-driven articulated modular snake robot," *IEEE/ASME Trans. Mechatron.* **24**(3), 893–901 (2019).

[8] X. Qi, H. Shi, T. Pinto and X. Tan, "A novel pneumatic soft snake robot using traveling-wave locomotion in constrained environments," *IEEE Rob. Autom. Lett.* **5**(2), 1610–1617 (2020).

[9] M. Luo, R. YAn, Z. Wan, Y. Qin, J. Santoso, E. H. Skorina and C. D. Onal, "OriSnake: Design, fabrication, and experimental analysis of a 3-D origami snake robot," *IEEE Rob. Autom. Lett.* **3**(3), 1993–1999 (2018).

[10] H. Jeon, Q. N. Le, S. Jeong, S. Jang, H. Jung, H. Chang, H. J. Pandya and Y. Kim, "Towards a snake-like flexible robot with variable stiffness using an SMA spring-based friction change mechanism," *IEEE Rob. Autom. Lett.* **7**(3), 6582–6589 (2022).

[11] X. Hu, A. Chen, Y. Luo, C. Zhang and E. Zhang, "Steerable catheters for minimally invasive surgery: A review and future directions," *Comput. Assisted Surg.* **23**(1), 21–41 (2018).

[12] K. Yoshimitsu, T. Kato, S. Song and N. Hata, "A novel four-wire-driven robotic catheter for radio-frequency ablation treatment," *Int. J. Comput. Assisted Radiol. Surg.* **9**, 867–874 (2014).

[13] Z. Wang, T. Wang, B. Zhao, Y. He, Y. Hu, B. Li, P. Zhang and M. Meng, "Hybrid adaptive control strategy for continuum surgical robot under external load," *IEEE Rob. Autom. Lett.* **6**(2), 1407–1414 (2021).

[14] Y. Kim, S. Cheng, S. Kim and K. Iagnemma, "A stiffness-adjustable hyperredundant manipulator using a variable neutral-line mechanism for minimally invasive surgery," *IEEE Trans. Robot.* **30**(2), 382–395 (2013).

[15] J. Kim, S. Kwon, Y. Moon and K. Kim, "Cable-movable rolling joint to expand workspace under high external load in a hyper-redundant manipulator," *IEEE/ASME Trans. Mechatron.* **27**(1), 501–512 (2021).

[16] W. Xu, T. Liu and Y. Li, "Kinematics, dynamics, and control of a cable-driven hyper-redundant manipulator," *IEEE/ASME Trans. Mechatron.* **23**(4), 1693–1704 (2018).

[17] A. Kanada and T. Mashimo, "Switching between continuum and discrete states in a continuum robot with dislocatable joints," *IEEE Access* **9**, 34859–34867 (2021).

[18] J. Suh, J. Lee and D. Kwon, "Underactuated miniature bending joint composed of serial pulleyless rolling joints," *Adv. Robot.* **28**(1), 1–14 (2014).

[19] D. Zhang, Y. Sun and T. C. Lueth, "Design of a novel tendon-driven manipulator structure based on monolithic compliant rolling-contact joint for minimally invasive surgery," *Int. J. Comput. Assisted Radiol. Surg.* **16**, 1615–1625 (2021).

[20] J. Suh, K. Kim, J. Jeong and J. Lee, "Design considerations for a hyper-redundant pulleyless rolling joint with elastic fixtures," *IEEE/ASME Trans. Mechatron.* **20**(6), 2841–2852 (2015).

[21] A. Loeve, P. Breedveld and J. Dankelman, "Scopes too flexible. . .and too stiff," *IEEE Pulse* **1**(3), 26–41 (2010).

[22] P. Berthet-Rayne, K. Leibrandt, K. Kim, C. A. Seneci, J. Shang and G. Yang. "Rolling-joint Design Optimization for Tendon Driven Snake-like Surgical Robots." **In:** IEEE/RSJ International Conference on Intelligent Robots and Systems (IROS) (2018) pp. 26–41.

[23] H. B. Brown, M. Schwerin, E. Shammas and H. Choset. "Design and Control of a Second-generation Hyper-redundant Mechanism." **In:** 2007 IEEE/RSJ International Conference on Intelligent Robots and Systems (2007) pp. 2603–2608.

[24] Z. Li, L. Wu, H. Ren and H. Yu, "Kinematic comparison of surgical tendon-driven manipulators and concentric tube manipulators," *Mech. Mach. Theory* **107**, 148–165 (2017).

[25] R. J. Webster, J. M. Romano and N. J. Cowan, "Mechanics of precurved-tube continuum robots," *IEEE Trans. Robot.* **25**(1), 67–78 (2008).

[26] T. Mahl, A. Hildebrandt and O. Sawodny, "A variable curvature continuum kinematics for kinematic control of the bionic handling assistant," *IEEE Trans. Robot.* **30**(4), 935–949 (2014).

[27] M. M. Dalvand, S. Nahavandi and R. D. Howe, "An analytical loading model for *n*-tendon continuum robots," *IEEE Trans. Robot.* **34**(5), 1215–1225 (2018).

[28] K. Kim, H. Woo and J. Suh. "Design and Evaluation of a Continuum Robot with Discreted Link Joints for Cardiovascular Interventions." **In:** 7th IEEE International Conference on Biomedical Robotics and Biomechatronics (Biorob) (2018) pp. 627–633.

[29] M. Hwang and D. Kwon, "K-FLEX: A flexible robotic platform for scar-free endoscopic surgery," *Int. J. Med. Rob. Comput. Assisted Surg.* **16**(2), e2078 (2020).

[30] H. Dehghani, S. Farritor, D. Oleynikov and B. Terry, "Automation of suturing path generation for da vinci-like surgical robotic systems," *Front. Biomed. Devices* **40789**, V001T07A008 (2018).

[31] S. A. Pedram, C. Shin, P. W. Ferguson, J. Ma, E. P. Dutson and J. Rosen, "Autonomous suturing framework and quantification using a cable-driven surgical robot," *IEEE Trans. Robot.* **37**(2), 404–417 (2020).

[32] C. Shin, P. W Ferguson, S. A. Pedram, J. Ma, E. P. Dutson and J. Rosen. "Autonomous Tissue Manipulation Via Surgical Robot Using Learning Based Model Predictive Control." **In:** International Conference on Robotics and Automation (ICRA) (2019) pp. 3875–3881.

[33] Z. Li, H. Ren, P. W. Y. Chiu, R. Du and H. Yu, "A novel constrained wire-driven flexible mechanism and its kinematic analysis," *Mech. Mach. Theory* **95**, 59–75 (2016).

[34] H. M. Le, T. N. Do and S. J. Phee, "A novel constrained wire-driven flexible mechanism and its kinematic analysis," *Sens. Actuat. A Phys.* **247**, 323–354 (2016).

[35] D. C. Friedman, T. S. Lendvay and B. Hannaford, "Instrument failures for the da Vinci surgical system: A Food and Drug Administration MAUDE database study," *Surg. Endosc.* **27**, 1503–1508 (2013).

https://doi.org/10.1017/S0263574725102452 Published online by Cambridge University Press

[36] G. Qin, A. Ji, Y. Cheng, W. Zhao, H. Pan, S. Shi and Y. Song, "A snake-inspired layer-driven continuum robot," *Soft Robot.* **9**(4), 788–797 (2022).
[37] D. Yoshikawa, M. Shimizu and T. Umedachi, "A single motor-driven continuum robot that can be designed to deform into a complex shape with curvature distribution," *ROBOMECH J.* **10**(1), 18 (2023).
[38] K. Oliver-Butler, J. Till and C. Rucker, "Continuum robot stiffness under external loads and prescribed tendon displacements," *IEEE Trans. Robot.* **35**(2), 403–419 (2019).
[39] K. Xu, J. Zhao and M. Fu, "Development of the SJTU unfoldable robotic system (SURS) for single port laparoscopy," *IEEE/ASME Trans. Mechatron.* **20**(5), 2133–2145 (2015).
[40] H.-T. Ryu, S.-M. Oh, K. Tae and B.-J. Yi, "DNA-helix inspired wire routing in cylindrical structures and its application to flexible surgical devices," *Soft Robot.* **9**(2), 337–353 (2022).

Cite this article: B. Lu, S. Wang and L. Pan (2025). "A cable-based synergy drive approach for variable curvature snake-like robots", Robotica **43**, 3346–3365. https://doi.org/10.1017/S0263574725102452

https://doi.org/10.1017/S0263574725102452 Published online by Cambridge University Press